Tellus SERIES A DYNAMIC METEOROLOGY AND OCEANOGRAPHY
PUBLISHED BY THE INTERNATIONAL METEOROLOGICAL INSTITUTE IN STOCKHOLM

Dynamical system analysis of a low-order tropical cyclone model

By DARIA SCHÖNEMANN* and THOMAS FRISIUS,
Junior Research Group Dynamical Systems, KlimaCampus, University of Hamburg, 20144, Hamburg, Germany

(Manuscript received 21 April 2011; in final form 30 November 2011)

ABSTRACT

Tropical cyclone dynamics is investigated by means of a conceptual box model. The tropical cyclone (TC) is divided into three regions, the eye, eyewall and ambient region. The model forms a low-order dynamical system of three ordinary differential equations. These are based on entropy budget equations comprising processes of surface enthalpy transfer, entropy advection, convection and radiative cooling. For tropical ocean parameter settings, the system possesses four non-trivial steady state solutions when the sea surface temperature (SST) is above a critical value. Two steady states are unstable while the two remaining states are stable. Bifurcation diagrams provide an explanation why only finite-amplitude perturbations above a critical SST can transform into TCs. Besides SST, relative humidity of the ambient region forms an important model parameter. The surfaces that describe equilibria as a function of SST and relative humidity reveal a cusp-catastrophe where the two non-trivial equilibria split into four. Within the model regime of four equilibria, cyclogenesis becomes very unlikely due to the repelling and attracting effects of the two additional equilibria. The results are in qualitative agreement with observations and evince the relevance of the simple model approach to the dynamics of TC formation and its maximum potential intensity.

Keywords: tropical cyclone dynamics, potential intensity and intensification, bifurcations and multiple equilibria

1. Introduction

A tropical cyclone (TC) can be considered in an idealised sense as an autonomous dynamical system. Although it is possible to simulate TCs in numeric models quite accurately, only little is known about their dynamical system characteristics. These characteristics are important to find out how often TCs appear and which intensity they may reach under different climate conditions. Our aim is to gain more understanding of the dynamical system TC using a hierarchy of models. In this contribution, we start with a highly simplified low-order model to grasp its dynamics.

Knowledge on the dynamical system properties of TCs helps to understand and judge the impact of climate change on their potential intensity (PI) and frequency of occurrence. It is still not clear how TCs react to global warming. Swanson (2008) found in observations a non-local response, pointing out that TC activity is correlated to relative sea surface temperature (SST) (i.e. local minus global mean SST). This suggests that besides local SST, also the environmental atmospheric stratification is crucial for TC dynamics because the latter is possibly influenced by the global mean SST.

It has been hypothesised that tropical cyclones can be understood as a stable branch occurring beyond a subcritical saddle node bifurcation at a certain SST. The other unstable branch after the bifurcation is associated with smaller but finite wind speeds that must be exceeded initially for the excitation of tropical cyclogenesis. Therefore, it could explain why not all initial perturbations develop into TCs. It remains unclear, why such a bifurcation should occur and what physical processes are responsible for this. Tang and Emanuel (2010) have shown that entrainment of low-entropy air towards the centre may form an obstruction to TC formation and intensification. They found a ventilation threshold, i.e. a bifurcation for steady-state solutions in their model. Emanuel (1989) demonstrated with a simplified axisymmetric model that import of low-entropy air into the boundary layer by shallow clouds or precipitation induced downdrafts can provide reasons for the finite amplitude nature of tropical cyclogenesis. Frisius and Hasselbeck (2009) found with more complex models the importance of precipitating

*Corresponding author.
email: Daria.Schoenemann@zmaw.de

Citation: Tellus A 2012, **64**, 15817, DOI: 10.3402/tellusa.v64i0.15817

downdrafts for suppression of initial perturbations. Therefore, it is likely that such processes are an essential ingredient for realistic dynamical system characteristics.

In this study, we investigate the dependency of TC intensity on SST and different factors that determine the entrainment of low-entropy air such as relative humidity in the catchment area of a TC and shallow convection within the ambient region. With regard to SST, it is found that the model indeed reproduces a subcritical bifurcation as hypothesised earlier by Emanuel and Nolan. Furthermore, we detect an amplitude threshold for the generation of a TC within a certain regime depending on SST and the mentioned entrainment factors. The threshold disappears for enhanced SST values and decreased entrainment of low-entropy air via secondary circulation in the vertical–radial plane. In turn, TCs of relatively high intensity can develop from an initial state very close to that at rest. The whole regime also proves to be sensitive to parameters constituting the convective exchange within the catchment area in the environment of the storm.

The remainder of this article is organised as follows: The conceptual model and the processes included are presented in section 2. In section 3, the TC state of the model is estimated and analysed. Section 4 shows and discusses the models' equilibria, their stability and bifurcations with regard to different parameters. In section 5, cyclogenesis mechanisms in the box model and its transient dynamics are investigated. Concluding remarks are given in section 6.

2. Model formulation

The model is based on the assumption of an axisymmetric vortex and is formulated in cylindrical coordinates. The TC is divided into three regions above the boundary layer: (i) eye, (ii) eyewall and (iii) outer region (see Fig. 1). The dynamical system is described by three autonomous ordinary differential equations and contains inhibiting processes. Therefore, not only the most intense states are considered but also the transient dynamics of development. The eye is assumed to develop passively with the eyewall and is treated as a solid body in rotation. Angular momentum surfaces form the boundaries of the eyewall. Within the Ekman layer, the outer eyewall boundary is located at the radius of maximum winds (RMW). Idealised axisymmetric model simulations reveal that the angular momentum at the RMW remains roughly constant during tropical cyclogenesis (see Appendix). For the model formulation, it is useful to introduce the so-called potential radius:

$$R = \sqrt{r^2 + \frac{2vr}{f}} = \sqrt{\frac{2m}{f}}, \tag{1}$$

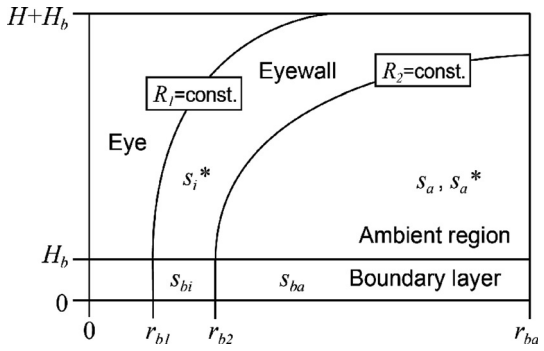

Fig. 1. Sketch of the low-order tropical cyclone model, where s denotes specific entropy, R the potential radius and r the physical radius. The index letters b, i and a stand for boundary layer, inner and ambient region, respectively. Evaluation at saturation is indicated by an asterisk. Further notation is given in the text.

where r denotes the physical radius, v the tangential velocity, f the Coriolis parameter and m the angular momentum density. We may interpret the model as a box model because the boundaries between the three regions are fixed in potential radius space.

2.1. Boundary layer flow

The dynamical equations are subject to the hydrostatic and the Boussinesq approximations. The latter leads to non-divergence of the radial–axial flow, i.e.

$$\frac{1}{r}\frac{\partial}{\partial r}(ru_b) + \frac{\partial w_b}{\partial z} = 0, \tag{2}$$

where u_b is the radial velocity, w_b the vertical velocity within the boundary layer and z the height. Because of the assumed non-divergence, we can introduce a mass-stream function Ψ having the following properties:

$$2\pi r\rho_b u_b = -\frac{\partial \Psi}{\partial z}, \quad 2\pi r\rho_b w_b = \frac{\partial \Psi}{\partial r}, \tag{3}$$

where ρ_b denotes the uniform density in the boundary layer.

The boundary layer is of a constant height H_b. We adopt the simple slab boundary layer model of Schubert and Hack (1983) in which a simplified aerodynamic drag law as a function of the balanced tangential wind at the boundary layer top ($z = H_b$) is assumed. The equation for boundary layer tangential wind v_b becomes

$$\zeta_b u_b = -\frac{C_D}{H_b}|v_b|v_b, \tag{4}$$

where C_D is the surface drag coefficient and ζ_b the absolute vorticity. Using this closure and ignoring vertical variation

of the horizontal wind components, we obtain the vertical velocity w_b at $z = H_b$ by vertical integration of the continuity equation (2). A comparison to eq. (3) leads to the following expression for the mass stream function at the top of the boundary layer:

$$\Psi_b = 2\pi r_b \rho_b C_D \frac{|v_b| v_b}{\zeta_b}. \tag{5}$$

The index b symbolises evaluation at $z = H_b$. We are aware of the limitations of this simple balanced boundary layer model [see Smith and Montgomery (2008)] but think it is appropriate in the context of a low-order model.

2.2. The eye

In the eye, we assume solid body rotation. Therefore, the tangential wind becomes

$$v_b = v_e \frac{r_b}{r_{b1}} = v_e \frac{R}{R_1}, \tag{6}$$

where r_{b1} and R_1 denote the physical radius and potential radius of the eye boundary, respectively (see Fig. 1). The velocity v_{b1} coincides with the eyewall velocity at $R = R_1$. The eye plays only a passive role in the present box model. This means, we neglect energy and mass fluxes from the eye into the eyewall. Hence, the model is not designed to investigate the role of eye–eyewall interaction processes. We skip this option because in this way, it is not necessary to determine mass fluxes, radial wind and entropy in the eye, and the thermodynamic budget equations to describe the system can be reduced to a number of three, as developed and defined in the following subsections.

2.3. The eyewall

Within the eyewall, we assume validity of the gradient wind balance, saturated pseudoadiabatic ascent and angular momentum conservation. These conditions allow for application of the thermal wind balance equation derived by Emanuel (1986), which relates specific saturation entropy s^* to angular momentum density m:

$$\frac{T_b - T}{m}\frac{ds^*}{dm} = 2\frac{T_b - T}{f^2 R^3}\frac{ds^*}{dR} = \frac{1}{r^2} - \frac{1}{r_b^2}, \tag{7}$$

where T denotes the temperature. Note that the saturation entropy s^* is only a function of angular momentum m. In eq. (7), the radius r as well as the temperature T is considered as a function of potential radius R and height z. The thermal wind balance equation (7) delivers the shape of the angular momentum surfaces as a function of R and the saturation entropy gradient at R. It can also be written as:

$$G(z - H_b) = \frac{1}{r(z)^2} - \frac{1}{r_b^2}, \tag{8}$$

with

$$G = \frac{2\Gamma}{f^2 R^3}\frac{ds^*}{dR}, \tag{9}$$

where Γ denotes the temperature lapse rate. The tropopause temperature T_t is presumed to be constant and independent of variations in the SST T_s, unless stated otherwise. The vertical temperature profile is approximated as linear with a constant lapse rate Γ throughout the troposphere. Using these assumptions, Γ is simply calculated from the difference between T_t and T_s divided by the tropopause height. This equation is evaluated at the inner and outer eyewall boundary, where the potential radius takes the values $R = R_1$ and $R = R_2$, respectively.

We approximate the radial entropy gradient at $R = R_2$ with a finite difference expression

$$\left.\frac{ds^*}{dR}\right|_{R=R_2} \approx -\frac{s_i^* - s_a^*}{\Delta R}, \tag{10}$$

where ΔR is the characteristic distance between the eyewall region and the outer region, s_i^* and s_a^* the mean saturated moist entropy anomaly of the eyewall and the outer region, respectively. So, we obtain at $R = R_2$:

$$G_2(z - H_b) = \frac{1}{r_2(z)^2} - \frac{1}{r_{b2}^2}, \tag{11}$$

with

$$G_2 = \frac{2\Gamma}{f^2 R_2^3}\frac{s_a^* - s_i^*}{\Delta R}. \tag{12}$$

Index 2 indicates evaluation at the outer eyewall boundary and, consequently, $r_2(z)$ denotes the physical radius of the angular momentum surface at $R = R_2$. Equation (11) prescribes the shape of the angular momentum surface at the outer eyewall boundary. However, there are still two unknowns, namely r_2 and r_{b2}. For closure, we assume that the mass M enveloped by this angular momentum surface is conserved (the reasonability of this assumption is addressed in section 2.5 and the Appendix). Using the simplifying assumption of a constant density ρ (Boussinesq

approximation), the mass M as a function of G_2 and r_{b2} becomes[1]:

$$M = \pi\rho \int_{H_b}^{H+H_b} r_2^2 dz = \frac{\pi\rho}{G_2} ln\left(1 + G_2 {r_{b2}}^2 H\right). \quad (13)$$

A more detailed derivation of eq. (13) is given in Frisius (2005). With this relation, we can determine the physical radius r_{b2} and tangential wind speed v_{b2} [see eq. (1)] at the outer eyewall boundary by the following equations:

$$r_{b2} = \sqrt{\frac{1}{G_2 H}\left[exp\left(\frac{G_2 M}{\pi\rho}\right) - 1\right]}, \quad (14)$$

$$v_{b2} = \frac{f}{2}\frac{R_2^2 - {r_{b2}}^2}{r_{b2}}. \quad (15)$$

By combination of eqs (9), (14) and (15), v_b can be computed as a function of the radial saturation entropy gradient at given potential radii. It can be seen that v_b decreases with decreasing ds^*/dR (not pictured here). We consider v_{b2} at R_2 as the maximum tangential velocity. Hence, the maximal ds^*/dR occurs at R_2 and must be smaller elsewhere. Looking at eq. (10), this condition is fulfilled when the radial entropy gradient at the inner edge of the eyewall ($R = R_1$) is calculated by:

$$\left.\frac{ds^*}{dR}\right|_{R=R_1} = -\frac{s_i^* - s_a^*}{\Delta R}\left(\frac{R_1}{R_2}\right)^{\kappa-1}, \quad (16)$$

where R_1 is the potential radius of the inner eyewall and κ is the power of the radial decrease ($\kappa \geq 1$) in saturation entropy with increasing distance from the RMW at R_2. In analogy to eq. (12) and under consideration of eq. (16), we obtain at the inner eyewall boundary:

$$G_1 = \frac{2\Gamma}{f^2 {R_1}^3}\frac{s_a^* - s_i^*}{\Delta R}\left(\frac{R_1}{R_2}\right)^{\kappa-1}. \quad (17)$$

To avoid that the eyewall forms a discontinuity, the angular momentum surfaces should not cross, i.e. G_2 must be equal to or greater than G_1. This also provides an upper limit for κ [$\kappa \leq 4$, see also Emanuel (1997)]. As mass fluxes from the eye into the eyewall are not considered in the box model (see section 2.2), we assume the mass of the eye enclosed by R_1 is conserved. With this simplification and the Boussinesq approximation, the eye mass in the free atmosphere above the boundary layer can be calculated analogously to eq. (13):

$$M_e = \pi\rho \int_{H_b}^{H+H_b} r_1^2 dz = \frac{\pi\rho}{G_1} ln\left(1 + G_1 {r_{b1}}^2 H\right), \quad (18)$$

From this, we can determine the physical radius r_{b1} and tangential wind speed v_{b1} at the inner eyewall boundary by the following equations:

$$r_{b1} = \sqrt{\frac{1}{G_1 H}\left[exp\left(\frac{G_1 M_e}{\pi\rho}\right) - 1\right]}, \quad (19)$$

$$v_{b1} = \frac{f}{2}\frac{R_1^2 - {r_{b1}}^2}{r_{b1}}. \quad (20)$$

2.4. The ambient region

Ascent does not take place in the ambient region that might be partially subsaturated. The mean specific entropy s_a is attributed to this region and is smaller than its saturation value s_a^*. These values are treated as constants. We intend to include prognostic equations for these entropies in the future. For the present low-order model, we only need to calculate the boundary layer mass flux from the ambient region into the eyewall region. By eq. (5), it does not only depend upon tangential wind v_{b2} and physical radius r_{b2} but also on absolute vorticity ζ_{b2}. To determine ζ_{b2}, a wind profile in the vicinity of r_{b2} must be known. We assume the profile to be in the shape of

$$v_b = \frac{v_{b2} {r_{b2}}^\beta}{r_b^\beta} \text{ for } r_b > r_{b2}, \quad (21)$$

where the exponent of radial decline β takes a value between 0.5 and 1.

Consequently, the absolute vorticity ζ_{b2} at the outer eyewall boundary becomes

$$\zeta_{b2} = f + (1 - \beta)\frac{v_{b2}}{r_{b2}}. \quad (22)$$

This expression can be substituted in eq. (5) to determine the mass transport into the eyewall region. The mass transport turns out to be sensitive to changes in β. A theoretically determined value by Emanuel (1986) becomes $\beta \approx 0.5$. For such a small value, however, the radial inflow to the eyewall region is too weak when we assume realistic values for the maximum tangential wind and the RMW. For example, assuming $v_{b2} = 50$ m s^{-1} and $r_{b2} = 10$ km and default values for the other model parameters (Table 1) gives a radial wind speed at $R = R_2$ of only about 2 m s^{-1}.

[1]Note that the coarse assumption of a constant density does not have a large impact on the tangential wind v_b, as detected by Frisius (2005). Furthermore, the relation ${r_{b2}}^2 = (GH)^{-1}$ is almost satisfied for a fully developed tropical cyclone so that the assumption of a constant density is not relevant in the mature state.

Table 1. Default model parameters

Notation	Value	Meaning
r_a	420 km	Outer radius where $p_s = p_{ref,s}$
r_{ba}	420 km	Outer radius of the ambient region
τ_E	48 h	Timescale, diabatic cooling
τ_C	4 h	Timescale, convective exchange
C_H	0.003	Transfer coefficient for enthalpy
C_D	0.003	Transfer coefficient for momentum
H	13.5 km	Tropopause height minus boundary layer height
H_b	1.5 km	Boundary layer height
f	$5 \times 10^{-5}\,\mathrm{s}^{-1}$	Coriolis parameter
κ	3	Eyewall entropy profile parameter
δ	0.25	Entrainment parameter
R_1	90 km	Inner potential radius of eyewall
R_2	180 km	Outer potential radius of eyewall
ΔR	30 km	Distance eyewall – outer region
ρ	0.45 kg m^{-3}	Mean density
ρ_b	1.1 kg m^{-3}	Mean boundary layer density
T_t	203.15 K	Tropopause temperature
T_s	301.15 K	Sea surface temperature
h_a	45%	Relative humidity, ambient region
p_a	500 hPa	Pressure level, ambient region
$h_{ref,b}$	80%	Relative humidity, boundary layer
p_{ref}	1000 hPa	Reference surface pressure
β	0.875	Tangential wind profile parameter

A maximum value of $\beta = 1$ on the other hand, results in an unrealistically high radial wind even twice as high as the tangential wind.

2.5. Thermodynamic equations

The low-order model is based on thermodynamic variables. All needed hydrodynamic variables can be deduced diagnostically from eqs (5), (12), (14), (15), (17), (19), (20) and (22). First, a prognostic equation for saturation entropy of the eyewall s_i^* is needed. It is changed by the mass flux from the boundary layer and diabatic processes such as radiation or turbulent mixing. The mass flux results from eq. (5) evaluated at $r = r_{b2}$. At the inner edge of the eyewall, we assume vanishing mass exchange with the eye. Furthermore, we presume that the inflow from the boundary layer into the eyewall is exactly compensated by the outflow in the upper troposphere. This implicates that the eyewall mass enclosed by angular momentum surfaces above the boundary layer is conserved. It is calculated in terms of potential radii:

$$M_i = M - M_e = M - \pi\rho H R_1^2 = \pi\rho H\left(R_2^2 - R_1^2\right). \qquad (23)$$

M_i given by eq. (23) is equivalent to the mass of the resting state with vertically oriented eyewall boundaries, i.e. $r_1 = R_1$ and $r_2 = R_2$. This assumption seems to be the most reasonable one because TCs typically grow in a horizontally uniform tropical atmosphere close to rest. As the model cyclone intensifies, the boundaries slant and the eyewall obtains the shape of a hyperboloid as drafted in Fig. 1.

The diabatic processes are parameterised with a linear relaxation to the state of the ambient region. Furthermore, we assume saturation, so that we can equate entropy with saturation entropy. Then, we obtain the following prognostic equation:

$$\frac{ds_i^*}{dt} = \Psi_{b2}\frac{s_{bi} - s_i^*}{M_i} + \frac{s_a^* - s_i^*}{\tau_E}, \qquad (24)$$

where s_{bi} is the mean specific entropy of the boundary layer beneath the eyewall, s_a^* the saturated moist entropy of the ambient region and τ_E the timescale for damping by diabatic cooling processes. The first term on the right-hand side (rhs) of eq. (24) represents the upward transport of high entropy air into the eyewall from the boundary layer beneath via the secondary circulation in the radial–vertical plane. Hence, it is related to deep convection in the inner region. The second term represents diabatic cooling.

Further equations for specific entropy of the boundary layer are needed. To calculate their tendencies, the mass of the boundary layer beneath the eyewall must be known. It is given by

$$M_{bi} = \pi\rho_b\left(r_{b2}^2 - r_{b1}^2\right)H_b, \qquad (25)$$

and may change in the course of development due to changes in r_{b2} and r_{b1}. The specific entropy is altered by surface heat fluxes and lateral inflow from the ambient region. These are applied by the following equation:

$$\frac{ds_{bi}}{dt} = \Psi_{b2}\frac{s_{ba} - s_{bi}}{M_{bi}} + \frac{C_H}{2H_b}\left(|v_{b2}| + |v_{b1}|\right)(s_{oi} - s_{bi}), \qquad (26)$$

where s_{ba} denotes the specific boundary layer entropy of the outer region,[2] C_H the surface transfer coefficient for enthalpy and s_{oi} the mean specific entropy at the ocean surface beneath the eyewall. Advective transport within the boundary layer via secondary circulation is represented by the first term on the rhs of eq. (26). The second term represents the surface transfer of latent heat into the boundary layer due to the prescribed thermodynamical disequilibrium between the sea surface and the atmospheric boundary layer. It has been simplified using an averaged wind speed in the box.

The specific boundary layer entropy s_{ba} outside the eyewall is altered by surface heat fluxes, radial advection,

[2]Strictly speaking, it should be the boundary layer entropy at $R = R_2$. However, we do not resolve the radial entropy profile in this low-order model and, therefore, assume a representative value for the whole box.

convective cooling and downwelling of low-entropy air from the free atmosphere above the boundary layer related to mass transfer along the secondary circulation. The following equation for the mean entropy s_{ba} in the outer region's boundary layer is introduced:

$$\frac{ds_{ba}}{dt} = \Psi_{b2}\frac{\delta s_a + (1-\delta)s_{ba0} - s_{ba}}{M_{ba}} + \frac{C_H}{2H_b}|v_{b2}|(s_{oa} - s_{ba}) + \frac{s_a - s_{ba}}{\tau_C}, \quad (27)$$

where $0 \leq \delta \leq 1$ is an entrainment parameter describing the entrainment of air into the ambient boundary layer. Taking $\delta = 1$ would be equivalent to the assumption that air transported by the secondary circulation came entirely vertically from the free atmosphere above the outer boundary layer, whereas taking $\delta = 0$ would correspond to assuming the entire air flew in sidewise from the far-field surroundings. In the following, we arbitrarily presume $\delta = 0.25$, i.e. 25% of the secondary circulation inflow into the outer boundary layer comes from above, and 75% laterally from the far-field beyond r_{ba}. s_{oa} and s_a are the mean specific entropies at the ocean surface and in the free atmosphere above the boundary layer, s_{ba0} is the far-field boundary layer entropy and τ_C is the timescale for exchange processes across the top of the boundary layer due to shallow convection, which is represented by the third term in eq. (27). The boundary layer mass in the ambient region is given by

$$M_{ba} = \pi\rho_b({r_{ba}}^2 - {r_{b2}}^2)H_b \quad (28)$$

and may change in the course of the development due to changes in r_{b2}. The radius r_{ba} determines the width of the ambient boundary layer and, therefore, its thermal inertia.

Yet, we have to determine the specific entropy s_o at the sea surface and the specific entropy s_a in the ambient region above the boundary layer, which will be done in the following. The sea surface entropy changes with time due to its dependence on surface pressure p_s. We use the approximated expression

$$s_o(T_s, p_s) = L_v\left(\frac{q_v^*}{T_s} - \frac{q_{v,ref}}{T_{ref}}\right) - R_d ln\left(\frac{p_s}{p_{ref}}\right) + c_p ln\left(\frac{T_s}{T_{ref}}\right), \quad (29)$$

where T_s denotes the SST and q_v the specific humidity. The index *ref* symbolises that the quantity is a constant reference quantity, and the asterisk denotes that the moisture variable is considered at saturation. The reference entropy s_{ref} coincides with the boundary layer entropy of the undisturbed environment, i.e. $s_{ba0} = 0$. Here, the temperature is identical to the SST T_s and the relative humidity takes the value $h_{ref,b}$. Therefore, we obtain

$$s_o = L_v\left(\frac{q_v^* - q_{v,ref}}{T_s}\right) - R_d ln\left(\frac{p_s}{p_{ref}}\right), \quad (30)$$

with the specific reference humidity $q_{v,ref}$.

We assume gradient wind balance to calculate the surface pressure p_s. Hence,

$$\frac{R_d T_s}{p_s}\frac{\partial p_s}{\partial r} = \frac{{v_b}^2}{r} + f v_b, \quad (31)$$

where R_d is the specific gas constant of dry air. A radial integration to infinity would lead to a diverging integral when the tangential wind takes a profile of the shape described by eq. (21). Therefore, the integration is only applied to a finite radius r_a where the surface pressure coincides with the reference value. By integration of eq. (31), we obtain

$$R_d T_s ln\left(\frac{p_{s2}}{p_0}\right) = -\frac{{v_{b2}}^2}{2\beta}\left[1 - \left(\frac{r_{b2}}{r_a}\right)^{2\beta}\right] + \frac{f v_{b2} r_{b2}}{1-\beta}\left[1 - \left(\frac{r_a}{r_{b2}}\right)^{1-\beta}\right]. \quad (32)$$

The surface pressure can be used to evaluate the entropy s_{o2} at the radius r_{b2}. For the surface entropy of the eyewall region, we assume $s_{oi} = s_{o2}$ and for the outer region $s_{oa} = (s_{o2} + s_{oa0})/2$, respectively, where s_{oa0} is the entropy at the surface for $R \to \infty$, namely

$$s_{oa0} = L_v\left(\frac{q_v^* - q_{v,ref}}{T_s}\right). \quad (33)$$

The undisturbed environment may be in a state of convective–radiative equilibrium, which is neutral to convective instability. It excludes an acquisition of kinetic energy from environmental convective available potential energy (CAPE). Observations indicate that CAPE does not vanish during the mature state of a TC (e.g. Sheets, 1969; Frank, 1977; Bogner et al., 2000) and increases with radial distance from the centre of the storm. Hence, assuming neutrality to convection, or more accurately to slantwise convection in potential radius space, may be appropriate for the eyewall region but not suitable for the ambient region. Therefore, we have investigated different cases that differ in their far-field equilibrium stratification:

- Case I, where we assume a constant lapse rate and boundary layer relative humidity ($h_{ref,b}$),
- case N1, where neutrality to convection is maintained by adjusting boundary layer relative humidity,

- case N2, where neutrality to convection is maintained by adjusting the temperature lapse rate,
- hybrid case H, which excludes convective instability, such as in case N2, but allows for stability in the ambient region such as in case I.

Convective instability in the far environment can only arise in case I. For case N2 and case H, we implement a lower convective damping, i.e. $\tau_C = 8$ h instead of $\tau_C = 4$ h. The reasons will be discussed in section 4. The entropy in the ambient region s_a is given by

$$s_a = L_v\left(\frac{q_{v,a}}{T_a} - \frac{q_{v,ref}}{T_{ref}}\right) - R_d ln\left(\frac{p_a}{p_{ref}}\right) + c_p ln\left(\frac{T_a}{T_{ref}}\right), \qquad (34)$$

where the index a denotes that the quantity is evaluated in the ambient region at a characteristic pressure level above the boundary layer p_a. The temperature T_a is calculated for a given pressure level p_a in analogy to a formula proposed by Reed and Jablonowski (2011) [see their eq. (5)]. We found that the difference between virtual and absolute temperature is relatively small in the calculation of T_a. It does not affect the outcoming tendencies discussed in this study. In the course frame of the box model, the difference between absolute and virtual temperature can therefore be neglected and T_a is determined sufficiently accurate by

$$T_a = T_s\left(\frac{p_a}{p_{ref}}\right)^{\frac{R_d\Gamma}{g}}, \qquad (35)$$

with the gravitational acceleration $g = 9.806$ m s^{-1}. Due to subsaturation in the ambient region on average, s_a is smaller than the corresponding saturation entropy s_a^*. As stated above, the boundary layer entropy in the far environment at the outer boundary of the box model s_{ba0} is put to zero. Consequently, the saturated entropy of the ambient region s_a^* must also be zero to provide for the case of convective neutrality. In this reference frame, s_a measured as an anomaly of s_{ba0} becomes negative. In case N1, we consider the moisture conditions of a pseudoadiabatically ascending parcel as the reference state and determine the relative humidity in the boundary layer analytically. In this way, it is assured that the value of the reference entropy equals that taken in the calculation of the surface entropy. In the non-neutral case I, s_a^* is calculated in reference to the prescribed conditions within the boundary layer beneath, and relative humidity in the boundary layer at r_{ba} is set to a value of 80%. In the other neutral case N2, T_a is not calculated from eq. (35). Instead, it is determined numerically to provide for neutrality such as in case N1 considered here (see above). In the hybrid case H, this will be done only where convective instability would occur. Elsewhere, the hybrid case H is identical to case I.

2.6. The thermodynamical system

The derivations of the previous subsections lead to a closed low-order TC model. The assumptions that were necessary to formulate the model are further substantiated in the Appendix by evaluating a TC simulation with a complex axisymmetric cloud model. The low-order model takes the form of a dynamical system with three autonomous ordinary differential equations for the three unknowns s_i^*, s_{bi} and s_{ba}. The equations are given by

$$\frac{ds_i^*}{dt} = \Psi_{b2}\frac{s_{bi} - s_i^*}{M_i} + \frac{s_a^* - s_i^*}{\tau_E}, \qquad (36a)$$

$$\frac{ds_{bi}}{dt} = \Psi_{b2}\frac{s_{ba} - s_{bi}}{M_{bi}} + \frac{C_H}{2H_b}(|v_{b1}| + |v_{b2}|)(s_{oi} - s_{bi}), \qquad (36b)$$

$$\frac{ds_{ba}}{dt} = \Psi_{b2}\frac{\delta s_a - s_{ba}}{M_{ba}} + \frac{C_H}{2H_b}|v_{b2}|(s_{oa} - s_{ba}) + \frac{s_a - s_{ba}}{\tau_C}. \qquad (36c)$$

In these equations, the mass stream function Ψ_{b2}, the tangential velocities v_{b1} and v_{b2}, the boundary layer masses M_{bi} and M_{ba}, and the specific entropies at the sea surface, s_{oi} and s_{oa}, can be written as a function of s_i^* by consideration of eqs (5), (12), (14), (15), (17), (19), (20), (22), (25) and (32). This is advantageous for the calculation of equilibria because we can derive a single equation for the equilibrium values of s_i^*.

The system dynamics depend on a number of model parameters. These are r_a, r_{ba}, τ_E, τ_C, C_H, C_D, H, H_b, f, κ, δ, R_1, R_2, ΔR, ρ, ρ_b, T_t, T_s, h_a, p_a, $h_{ref,b}$, p_{ref} and β (Table 1). Fixed parameter values for moisture and temperature at the respective pressure levels were chosen in close agreement to observational data (Jordan, 1958). The regions' extents in potential radius space, i.e. R_1 and R_2, were chosen in accordance with those of simulations with a high-resolution axisymmetric model (see Appendix).

3. Estimation of the TC state

Here, we consider the steady state solution that can be associated to a TC at its final intensity. For this purpose, we only consider the effects of transport via secondary circulation and latent heat transfer between ocean and atmosphere, and shallow convection. The obstructive effect of radiative cooling is neglected, i.e. we set $1/\tau_E = 0$. For a comparison with Emanuel's PI theory (E-PI, Emanuel, 1986), the existence of an eye is neglected by setting $R = 0$. The environmental CAPE should vanish as in E-PI, i.e. $s_{ba0} = s_a^* = 0$. In addition to this, we presume the ambient region to be saturated by setting $s_a = 0$ to have a relaxation towards a neutral state by shallow convection. Furthermore, the entrainment parameter δ is set to zero, i.e. entrainment of air along the secondary circulation does not enter from above the boundary layer but only from the far

environment. With these assumptions, we determine steady state solutions of the dynamical system (see eqs 36a, b, c) and solve the following equations:

$$0 = \Psi_{b2}\frac{s_{bi} - s_i^*}{M_i}, \tag{37}$$

$$0 = \Psi_{b2}\frac{s_{ba} - s_{bi}}{M_{bi}} + \frac{C_H}{2H_b}|v_{b2}|(s_{oi} - s_{bi}), \tag{38}$$

$$0 = -\Psi_{b2}\frac{s_{ba}}{M_{ba}} + \frac{C_H}{2H_b}|v_{b2}|(s_{oa} - s_{ba}) - \frac{s_{ba}}{\tau_C}. \tag{39}$$

The Coriolis force at $R = R_2$ is small compared to the centrifugal force for a TC vortex. In turn, the higher order term ${r_{b2}}^2$ becomes very small against ${R_2}^2$ and therefore negligible. Equations (15) and (22) can be simplified accordingly:

$$v_{b2} = \frac{f}{2}\frac{{R_2}^2}{r_{b2}}, \qquad \zeta_{b2} = (1-\beta)\frac{v_{b2}}{r_{b2}}. \tag{40}$$

Because $r_{b2} \ll r_2|_{z=H_b+H}$ for a fully developed TC, we can simplify the thermal wind balance equation [see eqs (11) and (12)] to

$$\frac{1}{{r_{b2}}^2} = \frac{2\Gamma H}{f^2 {R_2}^3}\frac{s_i^*}{\Delta R}. \tag{41}$$

Application of these approximations to eq. (5) leads to the following equation for the mass transport:

$$\Psi_{b2} = \frac{\pi\rho_b f {R_2}^2 C_D}{1-\beta} r_{b2}. \tag{42}$$

Then, evaluation of eqs (37) and (38) gives

$$s_i^* = s_{bi} = \frac{s_{ba} + \frac{C_H}{4C_D}(1-\beta)s_{oi}}{1 + \frac{C_H}{4C_D}(1-\beta)}. \tag{43}$$

Evaluation of eq. (39) using the approximation ${r_{ba}}^2 - {r_{b2}}^2 \approx {r_{ba}}^2$ for a fully developed cyclone leads to

$$s_{ba} = \frac{\frac{C_H}{4C_D}(1-\beta)s_{oa}}{\frac{{r_{b2}}^2}{{r_{ba}}^2} + \frac{C_H}{4C_D}(1-\beta) + r_{b2}\frac{H_b(1-\beta)}{R_2 f C_D}\frac{1}{\tau_C}}. \tag{44}$$

We see that shallow convection and entrainment are necessary to attain a boundary layer entropy below that of the sea surface in the outer region. Because $r_{b2} \ll r_{ba}$, the first term in the denominator of eq. (44) can be neglected. Only for very strong damping, i.e. smaller τ_C values, shallow convection provides the dominant contribution and the approximation

$$s_{ba} = \frac{C_H v_{b2}\tau_C}{2H_b}s_{oa} \tag{45}$$

holds. The physically valid solution for tangential wind with this approximation, negelecting the pressure dependence of surface entropy so that $s_{oi} = s_{oa} \equiv s_o$, becomes:

$$v_{b2} = \frac{C_H \Gamma H R_2 \tau_C s_o}{8H_b\Delta R(1 + \frac{C_H}{C_D}\gamma)} + \sqrt{\left[\frac{C_H\Gamma H R_2\tau_C s_o}{8H_b\Delta R(1+\frac{C_H}{C_D}\gamma)}\right]^2 + \frac{C_H}{C_D}\frac{\Gamma H R_2}{2\Delta R}\frac{\gamma s_o}{1+\frac{C_H}{C_D}\gamma}}, \tag{46}$$

where $\gamma = (1-\beta)/4$. This formula will be compared with that of E-PI theory (Emanuel, 1995). It predicts for maximum wind speed squared

$${v_{max,E}}^2 = \frac{C_H}{C_D}(T_s - T_{out})(s_{o2} - s_{b2}), \tag{47}$$

where s_{o2} and s_{b2} are the entropies of the surface and the boundary layer at $R = R_2$, respectively. s_{b2} is calculated in such a way that the relative humidity of the boundary layer equals environmental relative humidity, and the boundary layer temperature is identical to SST. T_{out} denotes the outflow temperature at the top lid of the model. Hence, the factor $T_s - T_{out}$ can be identified with ΓH in eq. (46). E-PI is proportional to $(C_H/C_D)^{1/2}$. A similar formula results for very small τ_C because then, the second term under the square root in eq. (46) dominates. This is consistent with E-PI because fixation of boundary layer relative humidity outside the eyewall by shallow convection is a crucial assumption in this theory. Figure 2 displays maximum tangential wind as a function of C_H/C_D using standard

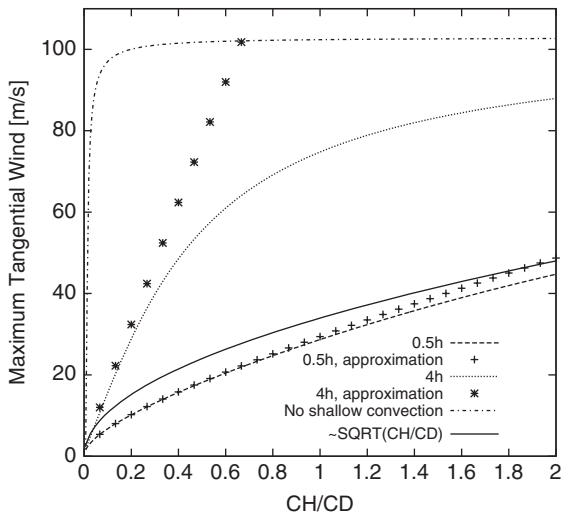

Fig. 2. Maximum wind speed of the TC state as a function of C_H/C_D for various timescales for shallow convective damping τ_C. The solid line displays $v_{b2} \propto \sqrt{C_H/C_D}$. The crosses and asterisks mark the analytical approximation given by eq. (46) for $\tau_C = 0.5$ h and $\tau_C = 4$ h, respectively.

parameters for different τ_C. For small τ_C (0.5 h), the increase in tangential wind with C_H/C_D is similar to the approximation (46) and it is roughly proportional to $(C_H/C_D)^{1/2}$. For larger damping timescales, eq. (46) becomes a poor approximation. When shallow convection is switched off, we obtain a very rapid increase of v_{max} with C_H/C_D and constancy afterwards in the box model. This behaviour seems rather unrealistic as it is unlike that of more complex numerical models (e.g. Emanuel 1995; Bryan and Rotunno, 2009a].

4. Equilibria, bifurcations and stability

As a standard parameter set of our model experiments, we use the values listed in Table 1. The simulations are based on this set as has been elaborated in section 2, unless stated otherwise.

First, equilibria are determined by an iterative procedure. The output of the standard simulation with gradual change in SST shows two up to four equilibria apart from the trivial solution, which is associated with an atmosphere at rest. Conducting a stability analysis by which eigenvalues from the respective Jacobian are numerically determined, we detect that the fourth or uppermost and the second equilibrium are stable (everywhere, apart from the A-regime that will be described below), whereas the first and third intermediate equilibria are unstable. The second equilibrium represents a low-pressure system of rather small intensity and the uppermost is associated with a TC. Figure 3 displays the maximum tangential wind of these equilibria as a function of SST for different values of relative humidity in the ambient region h_a. It can be seen from the 3-D plot (Fig. 3) and the regime diagrams (Fig. 4) that the number of equilibria strongly depends on h_a. In all cases, there is a threshold for the formation of cyclones, which is majorly determined by SST. Below a temperature of about 18°C, no stable low-pressure system would form in the model. Within a certain regime spanned by h_a and SST, we obtain two unstable equilibria, denoted by an A in the regime diagrams. The lower equilibrium acts as a repellor everywhere it exists. The upper one of these two equilibria exhibits the character of an unstable or negative fix point associated with two complex conjugated eigenvalues. For slightly higher temperatures and with increasing relative humidity in the ambient region, the fix point attractor becomes stable where the A-regime turns into the B1-regime. Two additional equilibria arise by a cusp catastrophe in the C-regime (Fig. 4) of which the upper one is stable (Fig. 3). The additional repellor imposes an amplitude threshold, i.e. it is obstructive to the formation of a storm reaching TC intensity. Only in the B2-regime, where we have two equilibria again, SST and h_a are sufficiently high for the formation of a TC from a small initial disturbance in an atmospheric state close to rest.

As can be seen from Fig. 5, the principal equilibrium structure as described above is qualitatively stable to changes in the exponent β that describes the radial decline of tangential wind velocity. However, there are quantitative changes and tendencies, i.e. the intensity of the TC decreases for lower β-values. This may be due to an enhanced mass transport across r_{b2} into the inner boundary layer with increasing β-values because Ψ_{b2} is approximately proportional to $(1-\beta)^{-1}$ [compare with eq. (42)]. Furthermore, the amplitude threshold is shifted to lower SSTs for lower β-values. This is true for both cases I and N1 pictured in Figs 3–5. Qualitatively and in terms of maximum wind speed for TCs, there is no visible difference between the non-neutral case I (Figs 3a, 4a and 5a) and case N1 (Figs 3b, 4b and 5b), whereas the amplitude threshold is sensitive to the stability conditions in the

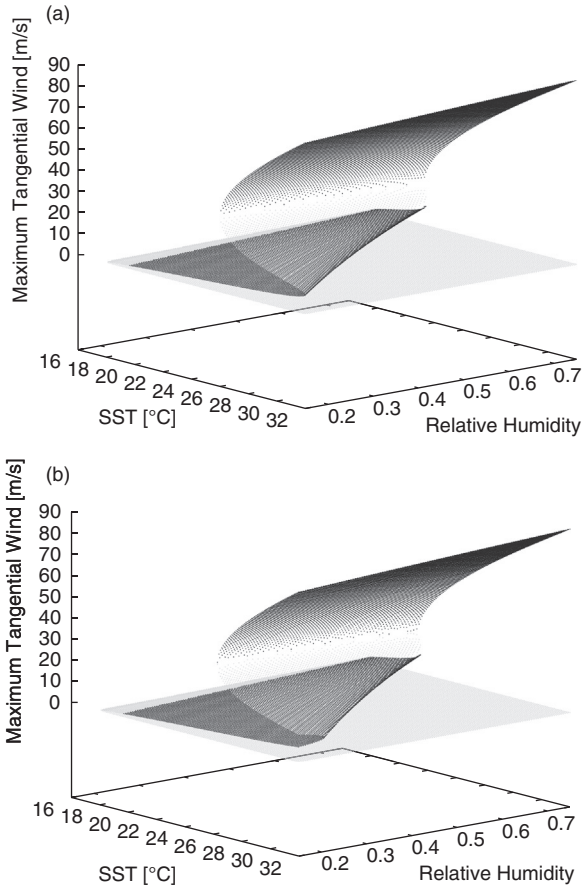

Fig. 3. Equilibrium solutions for maximum tangential wind as a function of T_s (°C) and h_a (fraction by one) for (a) the non-neutral case I and (b) case N1 under the assumption of convective neutrality. Stable equilibria are coloured in dark grey and unstable equilibria in brighter grey.

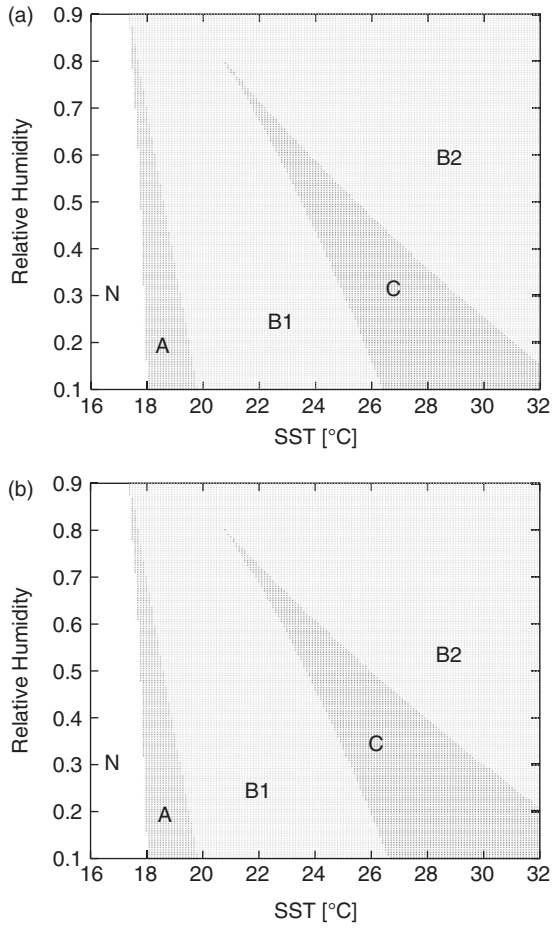

Fig. 4. Regime diagrams as a function of T_s (°C) and h_a (fraction by one) for (a) the non-neutral case I and (b) case N1 under the assumption of convective neutrality. The different regimes are labelled with different capital letters: The regime, where no stable low-pressure systems would form at all, is denoted as N-regime, in the A-regime we obtain two unstable equilibria, in the B-regimes (B1 and B2), the lower equilibrium is unstable and the upper is stable and in the C-regime, two unstable and two stable equilibria arise.

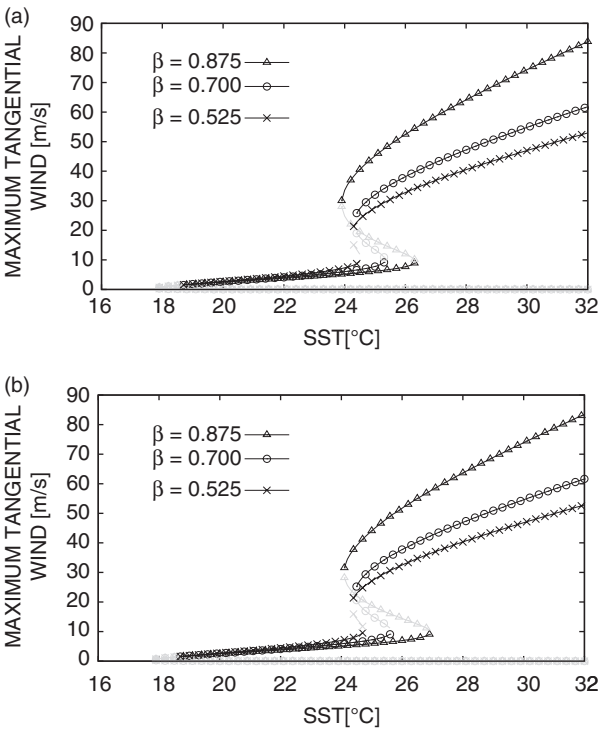

Fig. 5. Bifurcation diagrams of maximum tangential wind speed (m s^{-1}) as a function of T_s (°C) for different β-values and a relative humidity in the ambient region of $h_a = 45\%$ for (a) the non-neutral case I and (b) case N1 under the assumption of convective neutrality. Stable equilibria are coloured in dark grey and unstable equilibria in brighter grey.

ambient region. As can be seen from Fig. 4, the C-regime is broadened and the amplitude threshold is shifted towards higher temperatures in case N1. The quantitative differences between case I and case N1 disappear for $\delta = 1$ (not pictured here), presuming that air transported by the secondary circulation into the boundary layer comes entirely vertical from the ambient region above rather than its surroundings (in the figures shown here, δ equals 0.25 as stated in Table 1). The higher the amount of horizontal air transport into the boundary layer from the surroundings (i.e. the smaller δ), the larger becomes the difference between case I and case N1 with regard to the location and extent of the C-regime in the T_s–h_a-plane.

Model results from case I and case N1 are in qualitative agreement and display relatively small differences with regard to their quantitative behaviour. The decrease in boundary layer humidity in case N1 at higher SSTs compensates for the decreased dry static stability that we obtain when SST increases, whereas the tropopause temperature is held fixed. This way to maintain neutrality to convection results in unrealistically low values for relative humidity in the outer boundary layer at warm tropical SSTs. At $T_s \approx 25$°C, boundary layer humidity falls below 60% and it decreases even further for higher SSTs in case N1. On the other hand, relative humidity of the boundary layer at r_{ba} does not need to be calculated from other model variables in case I (see section 2.5). Instead, a fixed value of $h_{ref,b} = 80\%$ is chosen in case I, i.e. changes in dry static stability are not counteracted by changes in boundary layer humidity to keep moist neutrality. For reasons of clarity, we relinquish a further discussion on results of case N1 in the following part of this section and only display results from case I. However, we note that the results obtained from case N1 exhibit the same

behaviour as those from case I with regard to changes in the parameters investigated in this study.

Tropical cyclone intensity as well as the number of equilibrium solutions is sensitive to relative humidity in the ambient region above the boundary layer h_a (see above). The entropy in the ambient region depends on h_a [see eq. (34)]. Thereby, this model parameter highly influences the entrainment of low-entropy air from the ambient region into the boundary layer beneath via secondary circulation and shallow convection within the ambient region [see eq. (27)]. Another parameter, which determines the entrainment of low-entropy air into the boundary layer, is the timescale for convective damping τ_C [see eq. (27)]. As can be seen from Fig. 6, the strength of convective damping has a notable impact on TC intensity as well as the SST-amplitude threshold. For lower values in τ_C, i.e. enhanced shallow convective damping, maximum potential intensity (MPI) decreases and the amplitude threshold is shifted to higher SSTs. The sensitivity of the equilibrium structure to convective damping within the ambient region is further illustrated in regime diagrams in Fig. 7. The formation threshold is hardly affected by changes in τ_C, whereas the amplitude threshold is shifted to higher SSTs and relative humidity in the ambient region.

In Case N2, we make use of another possibility to ensure neutrality with respect to convection. In difference to case N1, the temperature stratification is corrected, whereas the boundary layer relative humidity $h_{ref,b}$ is kept constant. Instead of using eq. (35), the temperature T_a is determined iteratively, so that s_a^* becomes zero. The lapse rate Γ has been corrected accordingly. In Case I, the vertical temperature difference between T_s and T_a increases by definition with increasing SST, whereas T_t is treated as constant and independent of T_s [see section 2.3 and eq. (35)]. By contrast in case N2, neutrality to convection is maintained

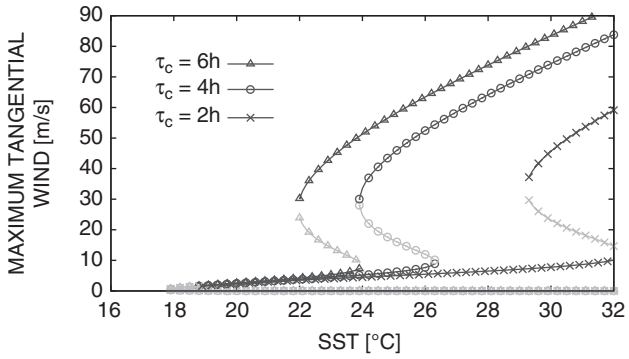

Fig. 6. Bifurcation diagram of maximum tangential wind speed (m s^{-1}) in case I as a function of T_s (°C) for different τ_C-values and a relative humidity in the ambient region of $h_a = 45\%$. Stable equilibria are coloured in dark grey and unstable equilibria in brighter grey.

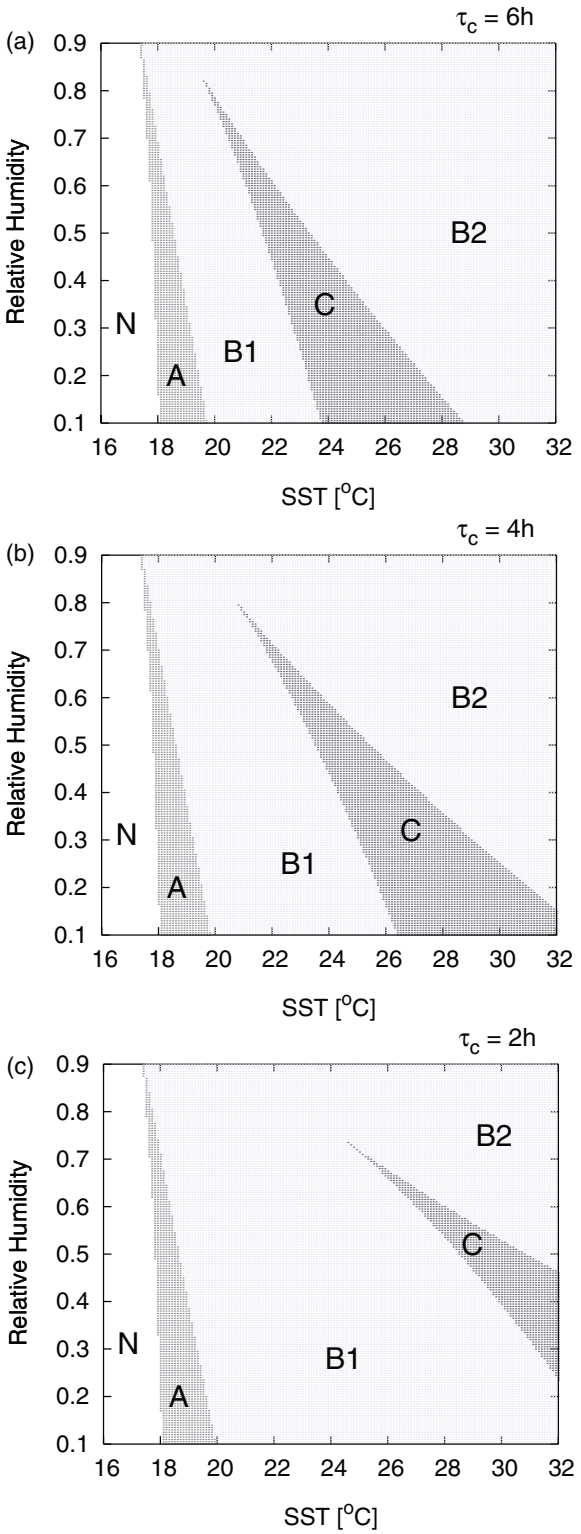

Fig. 7. Regime diagrams in case I as a function of T_s (°C) and h_a (fraction by one) for different timescales in convective damping: (a) $\tau_C = 6$ h, (b) $\tau_C = 4$ h and (c) $\tau_C = 2$ h. The different regimes are labelled as in Fig. 4.

by adjustment of T_a, which results in a decreased temperature difference between T_s and T_a (not pictured here), acting against instability. Model studies on global climate feedbacks reveal that the upper tropospheric temperature in the tropics increases in response to global warming and the tropospheric temperature lapse rate decreases (Hansen et al., 1984; Hegerl et al., 2007), which stabilises the vertical stratification. The configuration of case I allows us to investigate the behaviour of the dynamical system for different tropopause temperatures (Figs 8 and 9). The TC intensity increases with increasing difference between SST and tropopause temperature by lowering T_t (Fig. 8), and the amplitude as well as the formation threshold is shifted to lower SSTs (Fig. 9).

The equilibrium surfaces of maximum tangential wind and the regime diagram for case N2 are shown in Figs 10a and 11a, respectively. We see that non-trivial solutions appear for much lower SSTs, even below the freezing point, than in the other cases. For example, a maximum wind speed of about 33 m s^{-1} results for an SST of $T_s = 18°C$ and $h_a = 80\%$. Under these conditions, TCs do not occur in the real atmosphere. Therefore, we think that the assumption of convective neutrality cannot be applied in general. Looking at the regime diagram (Fig. 11a), we see that the equilibria exhibit a cusp bifurcation at $T_s \approx 10°C$ and $h_a = 50\%$. Beside its different position, the C-regime is also oriented in a different way compared to cases I and N1. Furthermore, the lower stable equilibrium becomes unstable for SSTs and low relative humidity, where the B1-regime again switches to the A-regime. A notable qualitative difference in comparison to case I and N1 is that the B2-regime narrows with increasing SST, i.e. the obstruction for tropical cyclogenesis becomes larger with

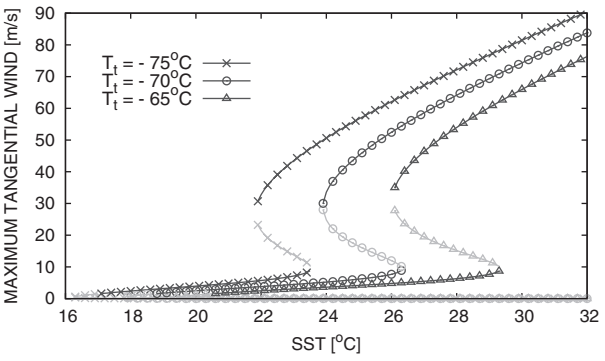

Fig. 8. Bifurcation diagram of maximum tangential wind speed (m s^{-1}) in case I as a function of T_s (°C) for different fix tropopause temperatures T_t and a relative humidity in the ambient region of $h_a = 45\%$. Stable equilibria are coloured in dark grey and unstable equilibria in brighter grey.

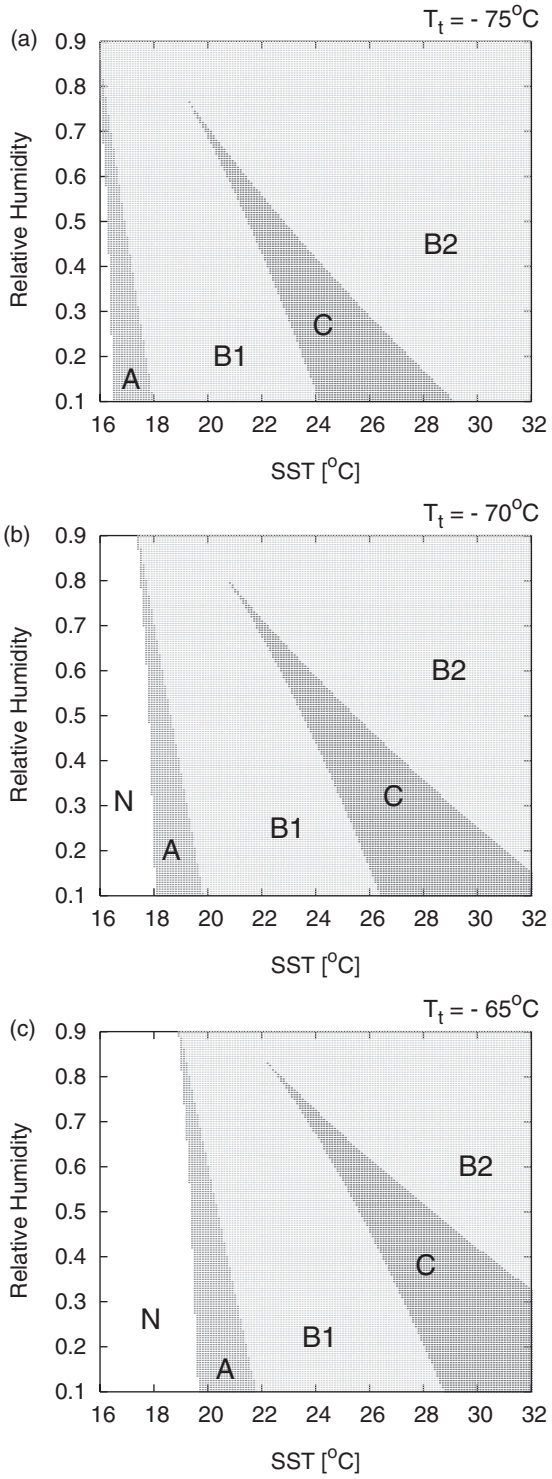

Fig. 9. Regime diagrams in case I as a function of T_s (°C) and h_a (fraction by one) for different tropopause temperatures: (a) $T_t = -75°C$, (b) $T_t = -70°C$ and (c) $T_t = -65°C$. The different regimes are labelled as in Fig. 4.

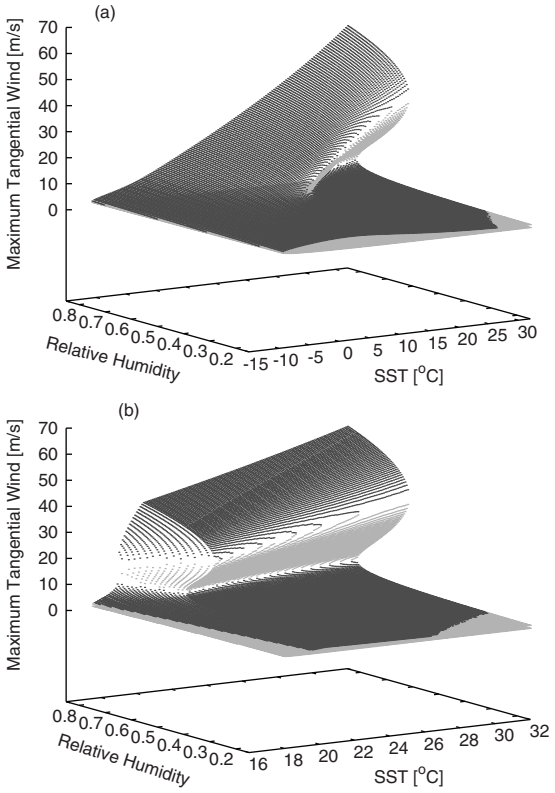

Fig. 10. Equilibrium solutions for maximum tangential wind as a function of T_s (°C) and h_a (fraction by one) with $\tau_C = 8$ h for (a) the neutral case N2 and (b) the hybrid case H. Stable equilibria are coloured in dark grey and unstable equilibria in brighter grey. Note that the SST-interval chosen in (a) to display case N2 extends into the unphysical range of temperatures below the freezing point.

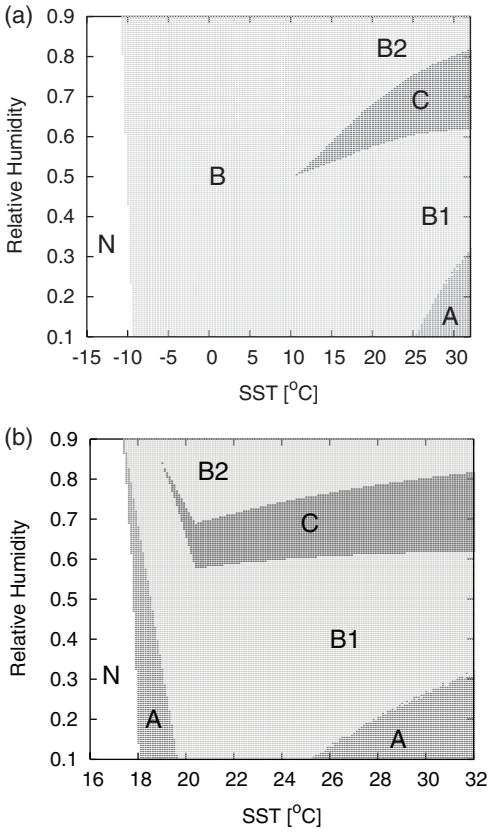

Fig. 11. Regime diagrams as a function of T_s (°C) and h_a (fraction by one) with $\tau_C = 8$ h for (a) the neutral case N2 and (b) the hybrid case H. The different regimes are labelled as in Fig. 4.

increasing SST in case N2. On the other hand, the steady state TC intensifies at higher SSTs. In Case N2, the N-regime arises only below an SST of about -10°C, where the validity of the model is rather questionable.

The results for the hybrid case H are displayed in Figs 10b and 11b. In this case, we have a clear SST formation threshold because in the regions with moist static stability, it coincides with case I, except for some small differences due to the different value for τ_C. Therefore, the A-regime occurs at both edges in the SST range shown in the regime diagram in case H. For larger SSTs, however, the regimes are (by definition) assembled identically to case N2 and quite differently from case I. So, a comparison to case H indicates that TC intensity in case I is sensitive to environmental CAPE. This is probably a consequence of the fact that the temperature T_a cannot change in time due to convective exchange. Possibly, case I would be more similar to the hybrid case, if a dynamical adjustment of T_a were allowed. Such an adjustment might be realisable by implementation of a prognostic entropy equation for the ambient region. However, this is beyond the scope of this study and will be subject to our future investigations. It becomes evident from Fig. 11b that tropical cyclogenesis is less likely for higher SSTs in the hybrid case H. This may seem to be surprising but is in qualitative agreement with recent climate change simulations that show a tendency towards increasing intensity and a decreasing frequency of occurrence of TCs in response to global warming (e.g. Bengtsson et al., 2007). An explanation for the increasing obstruction seems to be related to the secondary circulation that intensifies with increasing entropy difference between the atmosphere and the ocean. This enhances the injection of low-entropy air into the eyewall region and inhibits more efficiently the development of a TC.

Entrainment of low-entropy air by shallow convection in the ambient region, in addition to that by the secondary circulation, also has a highly impeding impact on TC formation in case H (Fig. 12). When we choose the same timescale for convective damping as depicted in Fig. 7a for case I ($\tau_C = 6$ h), the B2-regime exists only for relative humidity in the ambient region approximately equal or

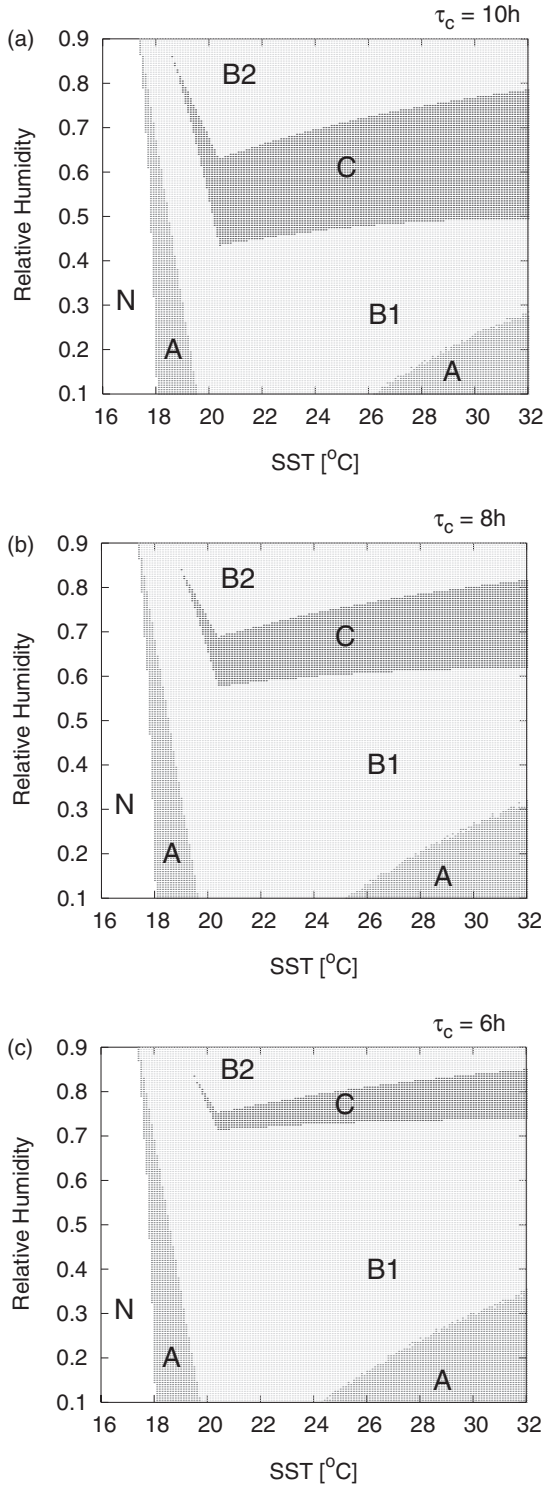

Fig. 12. Regime diagrams in case H as a function of T_s (°C) and h_a (fraction by one) for different timescales in convective damping: (a) $\tau_C = 10$ h, (b) $\tau_C = 8$ h and (c) $\tau_C = 6$ h. The different regimes are labelled as in Fig. 4.

even higher than that in the boundary layer beneath (Fig. 12c). Even if we take less than half the strength in convective damping as in case I, by setting τ_C to 10 h (Fig. 12a), a development of a TC from a small initial disturbance close to the state at rest still becomes only possible for relative humidity in the ambient region higher than ca. 63%, which is still about 18% higher, than the standard value we have chosen with regard to observational data at the 500 hPa-level (Jordan, 1958). To further abate the amplitude threshold with respect to h_a in case H, the entrainment of low-entropy air by convection within the ambient region must be further reduced by an increase in τ_C. For higher values in τ_C, the tendency of TCs becoming less likely with increasing SST is more pronounced (Fig. 12). On the other hand, in case I (see above) we found that TCs generally become more likely with both higher values in h_a and increased SSTs (Figs 3a and 4a), and the influence of h_a on the amplitude threshold gets smaller with decreased convective damping in the ambient region (Figs 6 and 7).

5. Cyclogenesis

5.1. Initial growth

To analyse the behaviour in the early phase of storm development, cyclogenesis in the box model is considered in a highly idealised way. In a state near to an atmosphere at rest, the eyewall region plays the role of a convective ring that eventually contracts and forms the eyewall of the fully developed TC. Such a cyclogenesis scenario is possible in an axisymmetric TC model. Regarding the growth of the TC, conditional instability of the second kind (CISK), [Charney and Eliassen (1964)] and wind-induced surface heat exchange (WISHE) [Emanuel (1997)] mechanisms may become crucial. The importance of these processes can be analysed in the box model by consideration of small amplitudes and neglecting obstructive processes, i.e. $\delta = 1/\tau_E = 1/\tau_C = 0$. Linearisation and combination of eqs (12), (14) and (15) with respect to the state at rest gives

$$v_b = \frac{\Gamma H}{2f\Delta R} s_i^*. \tag{48}$$

Using this approximation for v_{b2} and $\zeta \approx f$ in eq. (5), we obtain for the mass stream function

$$\Psi_{b2} = C_D \pi \rho_b R_2 \frac{\Gamma^2 H^2}{2f^3 \Delta R^2} s_i^{*2}. \tag{49}$$

The entropies at the sea surface and the mass M_{bi} are assumed to be constant. With these relations, the dynamical system becomes

$$\frac{ds_i^*}{dt} = \frac{F_C}{M_i} s_i^{*2}(s_{bi} - s_i^*), \tag{50}$$

$$\frac{ds_{bi}}{dt} = \frac{F_C}{M_{bi}} s_i^{*2}(s_{ba} - s_{bi}) + F_{Wi} s_i^*(s_{oi} - s_{bi}), \tag{51}$$

$$\frac{ds_{ba}}{dt} = -\frac{F_C}{M_{ba}} s_i^{*2} s_{ba} + F_{Wa} s_i^*(s_{oa} - s_{ba}). \tag{52}$$

where

$$F_C = C_D \pi \rho_b R_2 \frac{\Gamma^2 H^2}{2f^3 \Delta R^2}, F_{Wa} = C_H \frac{\Gamma H}{4f \Delta R H_b},$$

$$F_{Wi} = C_H \left[1 + \left(\frac{R_1}{R_2}\right)^{\kappa-1}\right] \frac{\Gamma H}{4f \Delta R H_b},$$

The atmosphere at rest (with $s_i^* = 0$) forms a steady state solution of the system. For this state, s_{bi} and s_{ba} can take arbitrary values because exchange with the sea surface vanishes. A stability analysis by linearisation of the system (50)–(52) reveals that the state at rest is dynamically indifferent. However, small perturbations may grow and eventually form a TC. This can be seen by solving eq. (50) for a prescribed boundary layer entropy $s_{bi,}$ which is positive and non-zero when the atmosphere is unstable to convection. Then, ignoring the third-order term on the rhs leads to the following solution:

$$s_i^* = \frac{s_{i0}^*}{1 - \frac{F_C}{M_i} s_{bi} t s_{i0}^*}, \tag{53}$$

which describes an intensification of the vortex with increasing growth rate from a small initial perturbation s_{i0}^*. This corresponds to cyclogenesis by the CISK mechanism, where the frictionally induced boundary layer inflow is responsible for latent heat release in the eyewall and thereby enhances the tangential wind. This in turn strengthens the inflow and, thereby, closes the feedback loop. We see that the intensification rate is proportional to the drag coefficient C_D. The growth stops when the eyewall-saturated moist entropy attains the value of the boundary layer.

For excitation of a pure WISHE feedback, the atmosphere must be neutrally stratified, i.e. $s_i^* = s_{bi}$. Convection is implicitly assumed to remove any convective instability immediately. Equating s_i^* with s_{bi} and linearisation of eq. (51) gives

$$\frac{ds_{bi}}{dt} = F_{Wi} s_{oi} s_{bi}, \tag{54}$$

The solution of this equation describes a perturbation intensifying with a growth rate $\sigma = F_{Wi} s_{oi}$ proportional to C_H.

We see that both CISK and WISHE feedbacks may be excited in the box model. Indeed, in the model these feedbacks act in a combined way. Combining the CISK and WISHE term by substitution of eq. (54) into the time derivative of eq. (50), neglecting third-order terms, we obtain the following differential equation:

$$\frac{d}{dt}\left(\frac{1}{s_i^{*2}} \frac{ds_i^*}{dt}\right) = \frac{F_C F_{Wi}}{M_i} s_{oi} s_i^*, \tag{55}$$

This equation shows that the intensification rate is proportional to $\sqrt{C_H C_D}$. The relevance of the combination of CISK and WISHE intensification mechanisms can be tested by variation of C_H and C_D as has been suggested by Craig and Gray (1996). Therefore, we performed various cyclogenesis simulations with the simplified system (50)–(52). All necessary model parameters are given in Table 1. Figure 13 displays time evolution of entropy s_i^* for various values of C_H and C_D. We clearly see that the growth rate is indeed a function of $\sqrt{C_H C_D}$, whereas the final intensity depends on C_H/C_D.

5.2. *Transient dynamics of amplification and equilibration*

The stability properties of the different equilibria are also reflected in the time development when we consider cyclogenesis, including all effects prescribed by the thermodynamic budget equations (eq. 36, section 2). For this purpose, the time integration is started close to or from initial conditions corresponding to the unstable equilibria

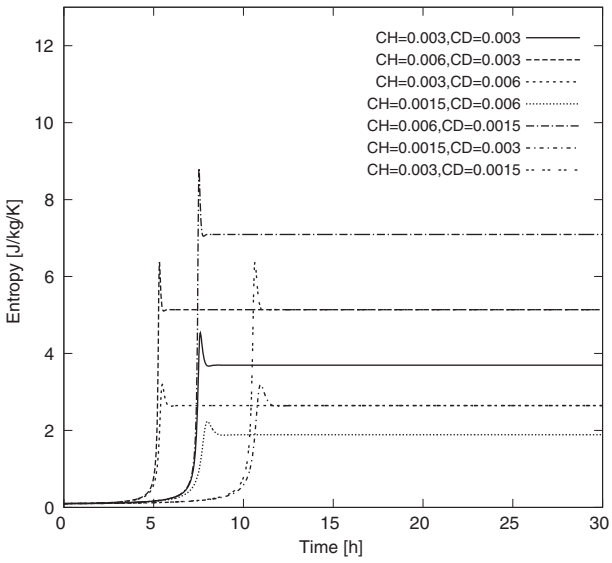

Fig. 13. Time evolution of entropy s_i^* for various transfer coefficients C_H and C_D. The curves display time integrations of the dynamical system (50)–(52), which is valid at small amplitudes.

(Fig. 14). Model experiments initialised by negative (positive) s_i^*-perturbations, inducing a negative (positive) deviation in velocity, with respect to a system repellor run into the respective lower (higher) stable equilibrium. As initialised with a negative perturbation with respect to the lowest unstable equilibrium, the system simply runs into the state of an atmosphere at rest. The smallest positive eyewall entropy perturbation introduced to the time experiments plotted in Fig. 14 equals 10^{-4} J kg^{-1} K^{-1} and is gradually doubled. The higher the magnitude of the perturbation, the faster does the system reach a stable state. At the beginning, the maximum tangential wind speed hardly increases for several days and it takes much longer than for higher perturbations until it intensifies with a relatively high rate. However, the maximum intensification rate is not visibly affected by the magnitude of the initial perturbation. Concerning TC genesis from very small initial perturbations (see Fig. 14b), our result is in qualitative agreement with that found earlier in a three-layer axisymmetric TC model by Anthes (1982).

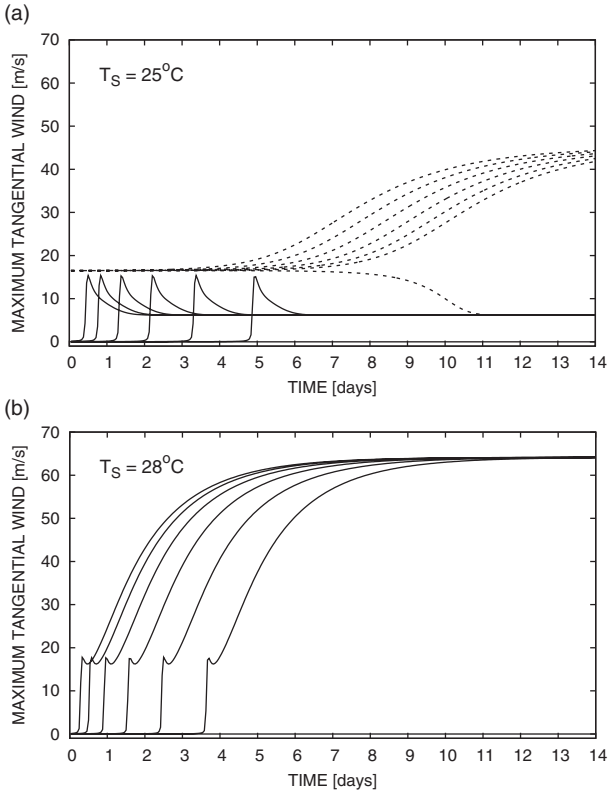

Fig. 14. Time development (in days) of v_{b2} (in m s^{-1}) in case I with $h_a = 45\%$ started near an unstable equilibrium for (a) $T_s = 25°C$ and (b) $T_s = 28°C$. Equilibrium solutions in the upper panel (a) are located in the C-regime (see Figs 3a and 4a), and model runs initialised by small perturbations with respect to the upper repellor are plotted with dashed lines and those started near the lower equilibrium are plotted with solid lines. In the lower panel (b), equilibrium solutions exist in the B2-regime with only one repellor. For each repellor, runs were initialised by one negative perturbation and six gradually increased positive perturbations.

As can be seen in Fig. 14b, the cyclone intensifies rapidly in the initial phase until it reaches a first maximum. Then, it slightly decays and further intensifies at a smaller rate than in the beginning. To some extent, this behaviour can be attributed to the action of the lower attractor that acts into the opposite direction of the upper attractor after the initial growth. The further we move away from the C-regime into the B2-regime (in T_s–h_a space), the weaker is the impeding effect of the lower attractor on TC formation and the higher is the intensification rate as the system develops from a weak storm into a tropical cyclone.

6. Discussion and conclusions

The dynamical system analysis of TCs in a conceptual box model reveals the existence of an SST threshold for the formation of cyclones under different conditions. We find that no cyclone would form below a certain SST. If neutrality to convection is maintained by moisture adjustment in the boundary layer (case N1), the SST formation threshold does not differ from that found in the case in which moist static instability was not excluded (case I).

The results of the neutral case N1 and the case, which allows for both negative and positive CAPE outside the eyewall (case I), are in good qualitative and quantitative agreement with regard to MPI, TC intensification and their sensitivity to the other model parameters investigated in this study. The type of neutralisation we obtain in case N1 corresponds to the neutralisation mechanism found from a correlation analysis of tropical soundings in regions with negative CAPE trends (DeMott and Randall, 2004). But in the box model, moisture adjustment (case N1) to maintain neutrality under decreased dry static stability results in unrealistically low values of boundary layer relative humidity over a warm tropical ocean. Quantitatively, this may possibly be due to the fact that we cannot look at the dynamically combined effect in the box model (i.e. we consider either a moisture or a lapse rate adjustment). On the other hand, when neutrality is kept by temperature adjustment in the ambient region as in case N2, the formation threshold would be shifted to SSTs below the freezing point, and storms of TC intensity already form over greatly colder water than in reality. This is also a result of E-PI theory excluding moist static stability of the atmosphere and premising a neutral ambient atmosphere instead. Observational studies give evidence for the existence of non-zero CAPE in the catchment area of a TC. Hurricane soundings computed from radiosonde measurements (Sheets, 1969) and measurements from dropwindsondes (Bogner et al., 2000) point to the existence of considerable

amounts of positive CAPE with increased radial distance from the centre of a mature TC. Analyses of satellite and radiosonde observations over areas with deep convection in the tropical Pacific exhibit the existence of positive CAPE for SSTs higher than 28°C and negative CAPE for SSTs below 27°C (Fu et al., 1994). Therefore, we also considered a hybrid case that allows for stability but prohibits instability by temperature adjustment (case H). Neutrality is probably a suitable assumption for regions characterised by strong convection because it contributes to the adjustment of the atmosphere towards a neutral state and in reverse, a reduced static stability facilitates convection.

The stability of the troposphere is to some extent determined by the temperature lapse rate. DeMott and Randall (2004) found that the correlation between temperature lapse rate, moisture content and CAPE depends on the sign of the trend in CAPE. Their results indicate that a decrease in CAPE is primarily driven by changes in the lapse rate, whereas increases in CAPE are chiefly driven by increasing moisture contents. Results from global climate models show that the lapse rate feedback in global warming scenarios, with enhanced mean SST, has a stabilising effect in the tropics by heating the upper troposphere at the expense of the surface (e.g. Hansen et al., 1984; Hegerl et al., 2007). This view is in accordance with the observed non-locality of TCs (Swanson, 2008). In this context, non-locality means that TC activity depends on the relation between local SST anomalies and global mean SST rather than only on local SST anomalies. With regard to the box model, this suggests that the tropopause temperature is mainly a function of global mean SST and that SST anomalies cause variations in static stability also crucial for TC activity. In the box model, this effect can be seen in both case N1, where decreased dry static stability is accompanied by a decrease in relative boundary layer humidity to maintain moist neutrality and in the non-neutral case I, where boundary layer humidity is held fixed. Presuming that changes in tropopause temperature are mainly controlled by changes in mean SST rather than local SST anomalies infers that the amplitude threshold of 26.5°C for TC development observed under present climate conditions is shifted under climate change.

Both, the hybrid case H and case I with no adjustment, display five different regimes with respect to the number of equilibrium states and their stability properties for different values in SST and relative humidity in the ambient region. By definition, case H and I are identical with regard to the formation threshold. Within a certain range in SST and h_a, we detect an additional repellor forming an amplitude threshold for the development of a TC. The amplitude threshold is sensitive to SST and entrainment of low-entropy air into the boundary layer. In case, we allow for positive CAPE in the ambient region, SST plays a more dominant role in setting the amplitude threshold than entrainment along the secondary circulation. Here, our model results imply that the frequency of occurrence of TCs rises with decreased entrainment of low-entropy air and locally increased SST.

In the hybrid case, the entrainment effect has a high impact on the amplitude threshold. TCs can only develop from small initial disturbances, when relative humidity in the ambient region is sufficiently high and convective damping within the ambient air is sufficiently low. In case H, TCs also become more intense but occur less frequently with increased SSTs when CAPE is zero. Here, neutrality is maintained by temperature adjustment resulting in a decreased vertical temperature gradient from the surface to mid-tropospheric levels at higher SSTs. Otherwise, instability to convection would rise over a warmer ocean as it does in case I. Because of this temperature adjustment, it was not possible here to probe the effect of a reduced or increased tropical tropopause temperature in response to global warming or cooling, combined with that of a regionally enhanced temperature gradient in the low-to-mid-tropospheric levels in response to a local increase in SST. Hence, in contrast to case I, we cannot discern the impact of local SST anomalies and non-local changes on SST in case H. Presumably, this is the major reason for the different results, we obtain in case I and H. This could be further investigated by testing the system behaviour for a dynamical temperature adjustment in case I. In the frame of the conceptual model, this may be feasible by implementation of an additional thermodynamic budget equation for the entropy in the ambient region, which is beyond the scope of this work but will be subject to a future study.

7. Acknowledgements

This work was supported by the DFG within the Cluster of Excellence 177 Integrated Climate System Analysis and Prediction (CliSAP). We would like to warmly thank our colleague Joachim Pelkowski for critical comments and helpful discussions on entropy calculation. Furthermore, we would like to thank one anonymous reviewer for his encouraging comments and Kerry Emanuel for his constructive criticism to improve our manuscript.

8. Appendix

A.1. Comparison with results of the axisymmetric cloud model HURMOD

The model formulation presented in section 2 is based on several assumptions. A comparison with the results of a complex model is useful to evaluate these assumptions. For this purpose, we analyse experiments simulated with the

axisymmetric cloud model HURMOD. The model and the simulations were described in detail by Frisius and Hasselbeck (2009). For the analysis we choose the experiment WARMRAIN. It is a simulation of genesis and equilibration of an axisymmetric tropical cyclone excluding the ice phase. In this case, the tropical cyclone reaches a quasi-steady state after equilibration. On the other hand, significant intensity fluctuations and eyewall replacement appear if the ice phase is included (experiment ICE). Such a complex behaviour is certainly beyond the scope of the simple box model. Therefore, this experiment is not suitable for the comparison.

Figure 15 displays vertical velocity at $z = 1250$ m and saturation entropy at $z = 5250$ m as a function of potential radius and time. We clearly see the eyewall region with positive vertical velocities in a potential radius range between 90 and 180 km. This region can even be identified in the growth period between 24 and 48 hours. The eyewall boundaries (to be defined as the 1 m s^{-1} isoline) migrate slowly towards larger potential radii but the eyewall width remains almost constant in potential radius space. The slow outward drift may be associated to the adjustment of the tropical cyclone to an equilibrium state with a certain radius of maximum wind. This hypothesis will be investigated in a subsequent study. Nevertheless, the assumption of constant boundaries for the eyewall seems reasonable to us in the context of a simple conceptual model. Consistent with the box model, saturation entropy does not vary appreciably with time outside the eyewall. The same is true for actual entropy (not shown). Cross sections of mass stream function and entropy time averaged over the period of 75–140 h are shown in Fig. 16. Obviously, the nearly vertically oriented isentropes in the eyewall support the assumption of slantwise neutrality used in the inner region of the box-model. The streamlines are also vertically oriented in the eyewall region with maximum vertical winds up to 8.4 m s^{-1} (not shown). The boundary layer inflow has a large vertical extent of about 2 km due to enhanced microturbulent vertical exchange. This value is a bit larger than that chosen for the box model solutions (1.5 km). The mass flux of approximately 1.5×10^9 kg s^{-1} into the eyewall is comparable to predictions from the box-model. Using the standard parameters (see table 1), $C_D = 0.0035$ (corresponds to HURMOD for a tangential surface wind of 60 m s^{-1}), $R_2 = 180$ km, $r_{b2} = 12$ km (estimated from HURMOD) we obtain $\Psi_{b2} = 1.88 \times 10^9$ kg s^{-1}. The entrainment of low entropy air in the boundary layer outside the eyewall is evident from the mass streamfunction field. The largest entropy values appear inside the eye. This is, however, energetically not relevant for the box-model.

Radial profiles of tangential wind at $z = 1250$ m for different times in the cyclogenesis phase are displayed in Fig. 17. An intensification of maximum tangential wind

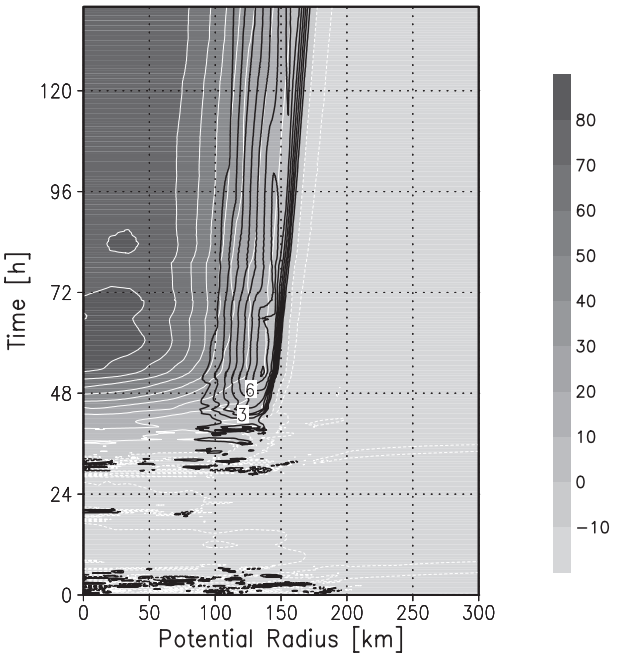

Fig. 15. Vertical velocity at $z = 1250$ m (black isolines, contour interval 1 m s^{-1}) and saturation entropy (shadings, J kg^{-1} K^{-1}) at $z = 5250$ m as a function of potential radius and time for the HURMOD experiment.

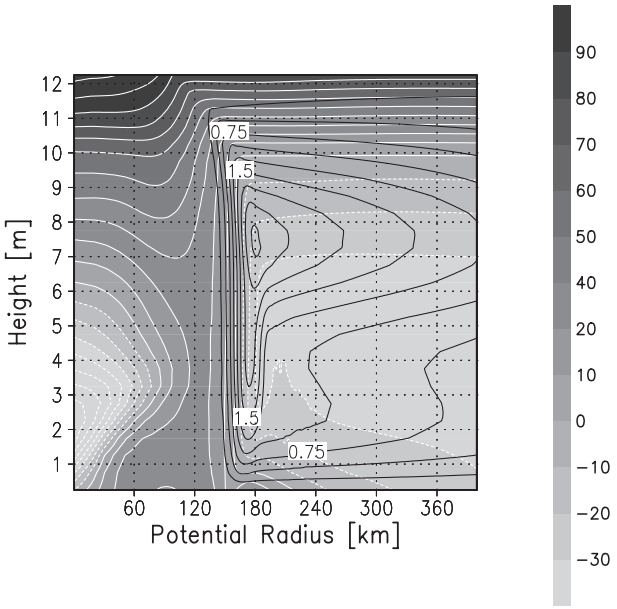

Fig. 16. Mass stream function (black isolines, contour interval 0.25×10^9 kg s^{-1}) and specific entropy (shadings, J kg^{-1} K^{-1}) time averaged over the period 75–140 h as a function of potential radius and height for the HURMOD experiment.

from 34 m s^{-1} to 65 m s^{-1} takes place within 12 hours while the radius of maximum winds migrates inward from $r = 12$ km to $r = 8$ km. The radius of maximum tangential wind and maximum gradient wind is located within the eyewall (not shown). Bryan and Rotunno (2009b) found in their axisymmetric model simulations at a higher resolution that the maximum gradient wind (denoted by $v_{g,max}$) is located close to the outer edge of the eyewall (see their Fig. 3). This is more consistent with the box-model and presumably a result of their finer model resolution. However, the figure also shows a decay of tangential wind with approximately $v \propto r^{-0.875}$ outside the eyewall. This is fulfilled best just outside the wind maximum near to the outer edge of the eyewall. Therefore, the choice $\beta = 0.875$ is in good agreement with HURMOD since the radial mass flux is calculated at this location. On the other hand, the displayed analytical profile $v \propto r^{-0.542}$ cannot be adapted to the HURMOD profiles indicating that the choice $\beta = 0.542$ does not agree with HURMOD results.

Finally, we have investigated the time variation of eyewall and eye mass in the HURMOD experiment. For this purpose, we prescribe the inner and outer eyewall boundaries by $R_1 = 90$ km and $R_2 = 180$ km, respectively. The eyewall region extends vertically from $z = 1$ km to $z = 11.5$ km. Looking at the time evolution of the eyewall and eye masses (Fig. 18), we see that the eyewall mass increases from 2.6×10^{14} kg to 4.2×10^{14} kg and afterwards it decreases again. The latter might be a result of the slow outward migration of the eyewall (Fig. 15). The variation of eyewall mass M_i has an effect on the growth rate and final intensity in the box-model. However, the assumption

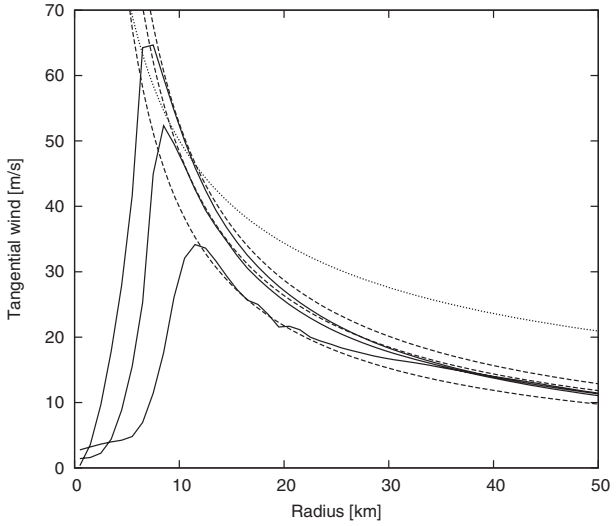

Fig. 17. Radial profiles of tangential wind at $z = 1250$ m for $t = 38$ h, $t = 44$ h and $t = 50$ h of the HURMOD experiment (solid lines). The dashed lines and dotted lines display the estimate for $v \propto r^{-0.875}$ and $v \propto r^{-0.542}$, respectively.

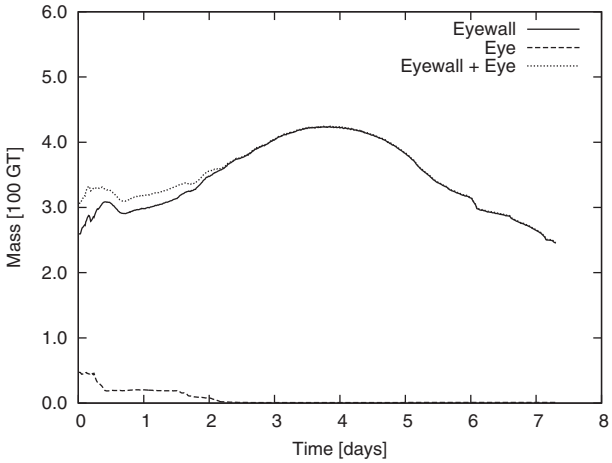

Fig. 18. Mass (in 100 gigatons) of the eyewall (solid line), eye (dashed line) and the sum of both (dotted line) as a function of time for the HURMOD experiment.

of constant eyewall mass is acceptable for the simple model since the variation remains below 50% with respect to the mean value. The change of eye mass is much more dramatic. At the beginning the eye region can of course not be associated with an eye. The term 'eye' just refers to the region $R < R_1$. The eye mass decays by more than one order of magnitude during the development from 4×10^{13} kg to 9×10^{11} kg. The reason for this dramatic decay seems to result from the fact that the R_1 surface is not an isentropic surface and more vertically oriented in HURMOD. This clear discrepancy with the box model is only of minor importance. Due to a relatively small eye mass, eyewall mass would only increase slightly if we would assume a vertical boundary between eye and eyewall instead of an isentrope. The only consequence of introducing a vertical boundary would be a slightly slower growth and weaker intensity of the tropical cyclone. The sum of eyewall mass and eye mass, i.e. $M = M_i + M_e$ is needed for the determination of the box model's tangential wind v_{b2} which in turn sensitively influences the mass-flux into the eyewall. The dependence of v_{b2} on M is weak for intense cyclones. In the growth stage M varies less than M_i due to the decay of eye mass M_e. Hence, the assumption of constant M is quite coarse but acceptable for the purpose of a conceptual model.

References

Anthes, R. L. 1982. Tropical cyclones: their evolution, structure and effects. *Meteorol. Monograph.* **19**(41), 101–102.

Bengtsson, L., Hodges, K. I., Esch, M., Keenlyside, N., Kornblueh, L. and co-authors. 2007. How may tropical cyclones change in a warmer climate? *Tellus* **59A**, 539–561.

Bogner, P. B., Barnes, G. M. and Franklin, J. L. 2000. Conditional instability and shear for six hurricanes over the Atlantic ocean. *Wea. Forcast*. **15**, 192–207.

Bryan, G. H. and Rotunno, R. 2009a. The maximum intensity of tropical cyclones in axisymmetric numerical model simulations. *Month. Wea. Rev*. **137**, 1770–1789.

Bryan, G. H. and Rotunno, R. 2009b. Evaluation of an analytical model for the maximum intensity of tropical cyclones. *J. Atmos. Sci*. **66**, 3042–3060.

Charney, J. G. and Eliassen, A. 1964. On the growth of the hurricane depression. *J. Atmos. Sci*. **21**, 68–75.

Craig, G. C. and Gray, S. L. 1996. CISK or WISHE as the mechanism for tropical cyclone intensification. *J. Atmos. Sci*. **53**, 3528–3540.

DeMott, C. A. and Randall, D. A. 2004. Observed variations of tropical convective available potential energy. *J. Geophys. Res*. **109**, D02102, doi: 10.1029/2003JD003784.

Emanuel, K. A. 1986. An air-sea interaction theory for tropical cyclones. Part I: steady-state maintenance. *J. Atmos. Sci*. **43**, 585–604.

Emanuel, K. A. 1989. The finite-amplitude nature of tropical cyclogenesis. *J. Atmos. Sci*. **46**, 3431–3456.

Emanuel, K. A. 1995. Sensitivity of tropical cyclones to surface exchange coefficients and a revised steady-state model incorporating eye dynamics. *J. Atmos. Sci*. **52**, 3969–3976.

Emanuel, K. A. 1997. Some aspects of hurricane inner-core dynamics and energetics. *J. Atmos. Sci*. **54**, 1014–1026.

Frank, W. M. 1977. The structure and energetics of the tropical cyclone: I. storm structure. *Month. Wea. Rev*. **105**, 1119–1135.

Frisius, T. 2005. An atmospheric balanced model of an axisymmetric vortex with zero potential vorticity. *Tellus* **57A**, 55–64.

Frisius, T. and Hasselbeck, T. 2009. The effect of latent cooling processes in tropical cyclone simulations. *Q. J. R. Meteorol. Soc*. **135**, 1732–1749.

Fu, R., Del Genio, A. D. and Rossow, W. B. 1994. Influence of ocean surface conditions on atmospheric vertical thermodynamic structure and deep convection. *J. Climate* **7**, 1092–1108.

Hansen, J., Lacis, A., Rind, D., Russell, G., Stone, P. and co-authors. 1984. Climate sensitivity: Analysis of feedback mechanisms. In *Climate Processes and Climate Sensitivity*, AGU Geophysical Monograph 29, Maurice Ewing Vol. 5. (eds. J.E. Hansen and T. Takahashi), American Geophysical Union, pp. 130–163.

Hegerl, G. C., Zwiers, F. W., Braconnot, P., Gillett, N. P., Luo, Y. and co-authors. 2007. Understanding and attributing climate change. In: *Climate Change 2007: The Physical Science Basis. Contribution of Working Group I to the Fourth Assessment Report of the Intergovernmental Panel on Climate Change* (eds. S. Solomon, D. Qin, M. Manning, Z. Chen, M. Marquis, K. B. Averyt, M. Tignor and H. L. Miller). Cambridge University Press, Cambridge, UK and New York, NY, USA.

Jordan, C. L. 1958. Mean soundings for the West Indies area. *J. Meteorol*. **15**, 91–97.

Reed, K. A. and Jablonowski, C. 2011. An analytic vortex initialization technique for idealized tropical cyclone studies in AGCMs. *Mon. Wea. Rev*. 139, 689–710.

Schubert, W. H. and Hack, J. J. 1983. Transformed Eliassen balanced vortex model. *J. Atmos. Sci*. **40**, 1571–1583.

Sheets, R. C. 1969. Some mean hurricane soundings. *J. Appl. Meteorol*. **8**, 134–146.

Smith, R. K. and Montgomery, M. T. 2008. Balanced boundary layers used in hurricane models. *Q. J. R. Meteorol. Soc*. **134**, 1385–1395.

Swanson, K. L. 2008. Nonlocality of Atlantic tropical cyclone intensities. *Geochem. Geophys. Geosyst*. **9**, Q04V01, doi: 10.1029/2007GC001844

Tang, B. and Emanuel, K. A. 2010. Midlevel ventilation's constraint on tropical cyclone intensity. *J. Atmos. Sci*. **67**, 1817–1830.